







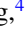

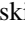
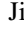

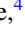



Insight into the physics of the $5f$ -band antiferromagnet U_2Ni_2Sn from the pressure dependence of crystal structure and electrical resistivity

Silvie Maskova-Cerna ¹, Alexandre Kolomiets ^{1,2}, Jiri Prchal ¹, Itzhak Halevy ³, Volodymyr Buturlim ¹, Mark Nikolaevsky ³, Oleksandra Koloskova ¹, Primoz Kozelj ⁴, Markus König ⁴, Martin Divis ¹, Leonid M. Sandratskii ¹, Jiri Kastil ⁵, Alexander V. Andreev ⁵, Eteri Svanidze ⁴ and Ladislav Havela ¹

¹Department of Condensed Matter Physics, Faculty of Mathematics and Physics, Charles University, Prague, Czech Republic

²Department of Physics, Lviv Polytechnic National University, Lviv, Ukraine

³Physics Department, Nuclear Research Centre Negev, Beer-Sheva, Israel

⁴Max-Planck-Institut für Chemische Physik fester Stoffe, Dresden, Germany

⁵Institute of Physics, Academy of Sciences, Prague, Czech Republic



(Received 8 October 2020; revised 22 November 2020; accepted 3 December 2020; published 6 January 2021)

A resistivity study of a single crystal of U_2Ni_2Sn has been performed at ambient pressure and under hydrostatic pressure up to $p = 3.3$ GPa. It revealed Fermi-liquid behavior accompanied by spin excitations with an energy gap $\Delta = 30\text{--}55$ K in the whole pressure range. The Néel temperature varies with pressure in a nonmonotonous way. It increases at the rate $dT_N/dp = +0.6$ K/GPa, and later, after passing through the maximum at ≈ 3 GPa, it starts to decrease quickly. High-pressure x-ray diffraction indicated that an orthorhombic distortion of the tetragonal structure takes place around the pressure of this T_N maximum. The computational study based on the density functional theory illustrates that the loss of magnetism in U_2Ni_2Sn with pressure is primarily due to $5f$ -band broadening, which results from the collapse of the U spacing within the U-U dimers.

DOI: [10.1103/PhysRevB.103.035104](https://doi.org/10.1103/PhysRevB.103.035104)

I. INTRODUCTION

The $5f$ -magnetism in light actinides is rather different from the magnetism in lanthanides based on localized $4f$ states as well as from the band magnetism of $3d$ metals. While still being essentially bandlike with the $5f$ states contributing to the Fermi level, strong spin-orbit interaction gives large orbital moments and pronounced magnetocrystalline anisotropy, both being very small in $3d$ systems. On the other hand, the degree of $5f$ delocalization can vary due to changes in crystal structure, chemical composition, and external variables such as pressure and magnetic field. As the itinerant and localized states cannot be reliably described on the same footing by existing *ab initio* computational approaches, the degree of delocalization or the verge of localization cannot be theoretically predicted for real materials. Hence, it is still mainly up to experimental studies to disclose the basic features of a particular metal, compound, or alloy. One issue is the lack of consensus about specific features indicating localization. Therefore, it is common to speak vaguely about the dual character of $5f$ systems [1], with some properties pointing to localization while others point to delocalization. In addition, the duality can also mean that an integer number of $5f$ electrons can be considered as localized, while the rest, typically noninteger, can be considered as itinerant [2]. The fact that not only do electronic properties interpolate between localized and delocalized limits, but novel exotic cooperative phenomena emerge along the way (unconventional superconductivity being the most striking one [3]), only emphasizes the peculiar nature of $5f$ electrons and their interactions.

The route to localization is typically marked by the quantum critical point, or, more generally, the point where static magnetism arises at or close to the $T = 0$ K limit, as the correlations strengthen and the $5f$ band becomes narrower. This so-called quantum criticality regime precedes the Mott transition, where the real localization happens. At present, the compounds located close to the quantum critical point or brought there by hydrostatic pressure represent truly exciting research areas [4]. On the other hand, the same pressure can have an opposite effect on materials located far away from the quantum criticality regime, in the range of strongly magnetic systems being close to the Mott transition [5,6]. Here the magnetic moments are rather stable with respect to the volume compression, while a reduction of the interatomic spacing can enhance significantly the temperatures of magnetic ordering, bringing the possibly useful features of the $5f$ magnetism closer to room temperature.

The present work focuses on the ternary U-based compound, U_2Ni_2Sn , located between the two limits. Since 1993 [7], it has been recognized that it is an antiferromagnet with the Néel temperature $T_N \approx 25$ K [8,9]. As a member of a large family of U_2T_2X compounds ($T =$ late transition metal; $X = Sn, In$) crystallizing in the tetragonal structure Mo_2FeB_2 (space group $P4/mbm$), which is a ternary variant of the U_3Si_2 type, it can be deduced that it is not very far from the onset of magnetism [10]. The borderline at which the stronger $5f$ - d hybridization suppresses antiferromagnetism is reached when going to the left in the $3d$ series. U_2Co_2Sn is on the nonmagnetic side [9,10]. Substitution of Fe for Ni in U_2Ni_2Sn suppresses antiferromagnetism on the level of

20%, and the weakly paramagnetic character at higher Fe concentrations demonstrates that the $3d$ magnetism does not visibly contribute to the magnetism of U_2Ni_2Sn [11].

The presence of sizeable U moments and, on the other hand, the proximity to the verge of magnetism and the Pauli paramagnetic state makes U_2Ni_2Sn an important system with the potential to provide additional insight into the magnetism of $5f$ systems. In particular, the study of magnetism under elevated pressure is an important experimental tool, representing one of the main goals of the present paper. We will mostly deal with the experimental study of electrical resistivity, which provides valuable information about the processes in the electronic system. Determination of the pressure-driven variations of the crystal structure proves to be an essential part of such a project.

The first electrical resistivity study [8] on a polycrystal with a poor residual resistance ratio ($\rho_{300\text{ K}}/\rho_0$), $RRR \approx 2$, showed a rather flat temperature dependence $\rho(T)$ in the paramagnetic state, with a broad maximum around $T \approx 70\text{ K}$, followed by a weakly negative slope on the high-temperature side. T_N manifests itself as a precipitous drop. A more detailed study on a sample with $RRR \approx 3$ [12] revealed that $\rho(T)$ below T_N tends first to increase with the final decrease to the residual resistivity ρ_0 starting a few degrees below T_N . A weak maximum just below T_N was also reported in another study [13], which, however, indicates a positive slope in the paramagnetic state. Because of cracks in the polycrystalline materials, none of the studies could determine the absolute values of resistivity.

All magnetically ordered U_2T_2X compounds are antiferromagnets. This may be arguably related to a complicated coordination of U atoms. U atoms form basal-plane sheets (interlaced with T-X sheets). Each U has one nearest neighbor in the sheet, while four more U atoms are somewhat farther apart. The nearest U neighbors are between the sheets in most cases. Therefore, it is likely that at least some of the inter-U exchange interaction favors an antiferromagnetic coupling. The direction of U moments is determined by the anisotropy. The usual rule of the easy magnetization direction being perpendicular to the nearest U-U links, stressing the role of two-ion anisotropy based on the $5f$ -bonding directions [14], works relatively reliably for the U_2T_2X compounds, frequently yielding U moments in the basal plane in an orthogonal pattern [10]. However, the unit cell of U_2Ni_2Sn is extremely elongated along c and contracted in the basal plane, more or less preserving the volume of its closest counterpart, U_2Ni_2In [7]. This brings about a situation in which the shortest U-U distance is between the basal-plane dimers, and the spacing along c is larger. It raises the question of whether the U moments could be reoriented from the basal plane into the c -axis. The powder neutron diffraction [15] suggested that this is not the case; however, the difference between different models was not large. Eventual success in single-crystal growth allowed us to determine the anisotropy of bulk magnetic properties, and the details of the magnetic structure gave unambiguously the c -axis alignment of U moments of $0.87\mu_B$, which are AF coupled both along c and within the basal plane, where moments of each of the four U atoms in one unit cell compensate each other. The propagation vector of the magnetic structure is $q = (0, 0, 1/2)$. The structure is robust

with respect to magnetic field H ; a cascade of metamagnetic transitions starts only at $\mu_0H = 30\text{ T}$ if applied along c . If H is perpendicular to c , no transition is found up to 60 T [16]. While an earlier specific-heat study of a polycrystal gave the Sommerfeld coefficient of electronic specific heat $\gamma = 172\text{ mJ/mol f.u. K}^2$ (1 f.u. contains two U atoms) [9], the single-crystal experiment gave the somewhat higher value $\gamma = 187\text{ mJ/mol f.u. K}^2$ [16]. Such a high value confirms the high density of the $5f$ states at E_F . It naturally does not reach 400 mJ/mol K^2 , assumed to be a heavy fermion threshold. On the other hand, the magnetic moments of almost $1\mu_B$ signal a significant exchange splitting, removing part of the high density of states from E_F . The generalized gradient approximation (GGA) and GGA + U calculations [17] revealed that the total moment is, as usual for U compounds, the difference between a larger orbital and an antiparallel smaller spin moment.

The aim of the present work is to determine the details of the electrical resistivity of U_2Ni_2Sn at ambient conditions and under applied hydrostatic pressure of several GPa in order to track the stability of U magnetic moments and the development of exchange interactions. Interpretation of the experimental data has been performed in conjunction with various first-principles calculations, providing information on the stability of U moments and exchange interactions as depending on lattice contraction caused by the applied pressure.

II. EXPERIMENTAL AND COMPUTATIONAL DETAILS

The single crystal, used previously in bulk magnetic and neutron diffraction studies [17], had been grown using the Czochralski method from a stoichiometric mixture of pure elements (99.9% U, 99.99% Ni, and 99.9999% Sn) in a tri-arc furnace with a water-cooled copper crucible under a protective argon atmosphere. A tungsten rod was used as a seed. The pulling speed was 10 mm/h . The phase purity and composition of the samples were checked by standard x-ray powder diffractometry and x-ray microanalysis. The backscattering x-ray Laue patterns revealed a good quality of the crystals. For the measurements of electrical resistivity and its anisotropy, two bars were cut from the same crystal and used in ambient pressure as well as high-pressure experiments. The bar dimensions were $0.75 \times 0.2 \times 0.2$ and $1.2 \times 0.4 \times 0.3\text{ mm}^3$ for the $i//[110]$ and $i//[001]$ measurements, respectively. The voltage contact separation was 0.2 and 0.3 mm , respectively, which results in at least 10% uncertainty of the absolute resistivity values considering the $25\mu\text{m}$ thickness of Pt voltage leads attached to the sample by spark welding.

In addition, we performed measurements on a microscale device made of U_2Ni_2Sn crystal using a plasma focused ion beam (FIB), with details of the procedure described previously [18]. The resulting microdevice is shown in Fig. 1. Panel (c) shows the current path, while the panel (d) indicates the voltage terminals. The advantage of such a device is a better defined geometrical factor determining the absolute value of resistivity, as well as better defined directionality of the electrical current, since the long dimension determining the current flow is much larger than both transverse directions. A disadvantage is the possibility of structural damage to the surface layer (typically only a few nm deep), as well as mechanical strain, induced by the device mounting procedure.

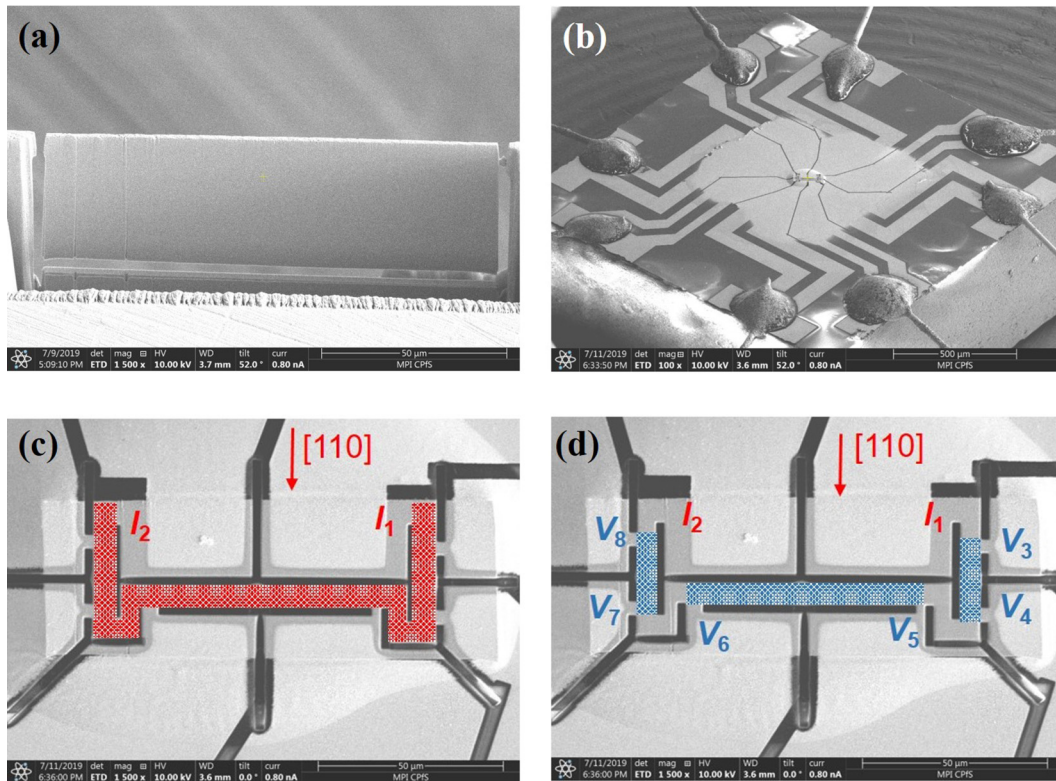


FIG. 1. (a) The undercut lamella connected to the parent crystal by a thin bridge. (b) The lamella placed on a substrate with prefabricated electric contact pads. (c),(d) Shape of the microscale device used for measurement. V and I are contacts for voltage and current, respectively. Panel (c) shows the current path, while (d) shows the voltage terminals.

The prepared device can be used to measure simultaneously the resistivity along as well as perpendicular to $[110]$.

Electrical resistivity measurements on the macroscopic samples were performed using the four-probe method simultaneously on the two bars. A magnetic field was applied along the $[001]$ direction, which is the easy-magnetization direction. In the case of a high-pressure experiment, the bars were mounted in proximity to the axis of a cell described below and to a magnet in order to assure maximum pressure and field homogeneity. The standard temperature range 2–300 K was in some cases extended using the ^3He insert of the Quantum Design Physical Property Measurement System (PPMS), reaching as low as 400 mK.

After the ambient pressure measurement, the high-pressure resistivity experiment was accomplished. For that, the samples were loaded into the hybrid two-layered CuBe/NiCrAl clamped pressure cell (C&T Factory Co., Ltd.) with a highest nominal pressure of 3 GPa [19]. Daphne 7373 oil was used as the pressure-transmitting medium [20], and thermally stabilized manganin wire was used to determine the pressure inside the cell at room temperature. The drop in pressure inside the pressure cell due to the cooling of the Daphne 7373 oil from room temperature to the lowest achieved temperature of $T = 2$ K was $\Delta p \approx 0.2$ GPa in the pressure range 0.0–2.2 GPa, and somewhat larger at elevated pressures, reaching as high as $\Delta p \approx 0.6$ GPa for 3.0 GPa [21]. The pressure values given in this work are room-temperature values. The cell is designed to fit inside the PPMS system, which provides temperatures

and magnetic fields in the range of 2–300 K and 0–14 T. The electrical transport option (ETO) was used to collect the data for the two samples, measured in the pressure experiment. The electrical resistivity measurements on the microdevice were also performed using the four-probe method in the Quantum Design PPMS in the temperature range 1.8–400 K and magnetic fields up to 9 T. The probing current with amplitude 1 mA and frequency 93 Hz was used. The measurement was performed both while cooling and heating, with no thermal hysteresis observed. The influence of the cooling/heating rate was tested as well. Again, no difference was observed.

The x-ray diffraction (XRD) patterns under high pressure were taken at room temperature with 2–3 GPa steps. A small amount of the sample (micron-sized powder) was loaded into a 301-steel gasket and placed in a Tel-Aviv design diamond anvil cell (DAC) with a pair of 500 μm culet-sized diamond anvils. Brilliant cut and Bohler-Almax design (BA) anvils were used. Si oil was loaded into the cell to act as a pressure medium, and ruby spheres were placed in the sample to be used as pressure calibrants. A Bruker microfocus x-ray source (I μ S 3.0) at the NRCN, with a Mo anode, created a monochromatic x-ray beam ($\lambda = 0.7107 \text{ \AA}$, Zr filter was used to avoid diffraction of the $K\beta$ radiation) that was focused on the sample. The beam's full width at half-maximum (FWHM), at the focal point, was 110 μm . A two-dimensional (2D) CMOS detector was used to measure the diffraction pattern. The DAC was placed with the BA anvil facing the detector to obtain a 70° aperture (i.e., a 2θ range of 0° – 35°). The entire setup was

held on a 2θ stage. The 2D data were converted to 2θ -intensity patterns by integrating over the Debye rings using FIT2D software [22]. All diffraction patterns were refined using MAUD software [23].

A suite of first-principles methods has been deployed to describe the magnetism of U_2Ni_2Sn and its underlying electronic structure at ambient and high pressures. Namely, we undertook a computational study based on the density functional theory (DFT) of equilibrium volume and electronic properties (mainly magnetism) using full potential methods, such as full potential local orbitals (FPLO) [24] and full potential linearized augmented plane waves plus local orbitals [(L)APW+lo], which is embedded in the WIEN2K program package [25]. The use of full potential methods is very important since the crystal structure at elevated pressures becomes orthorhombic and very anisotropic. The uranium $5f$ -states were treated as itinerant Bloch states in both methods. We used the fully relativistic Dirac four-component option in the FPLO calculations of electronic structure (non-spin-polarized), and the scalar relativistic option for the fixed spin moment (FSM) FPLO calculations. For testing purposes, the scalar relativistic calculations for both FPLO and (L)APW+lo were performed, and the same density of states at the Fermi level at experimental equilibrium volume confirmed the compatibility of both methods. For calculations with the FPLO code, we used the divisions $12 \times 12 \times 12$, $24 \times 24 \times 24$, and $36 \times 36 \times 36$ corresponding to 1728, 13824, and 46656 k -points in the Brillouin zone, respectively. The numbers of irreducible k -points were 343, 2197, and 6859. These numbers of k -points were sufficient to obtain converged density of electronic states (DOS) and the converged total energy in the FSM calculations.

The (L)APW+lo method was applied to determine the equilibrium lattice volume, which can be compared with the experimental value. More than 2200 augmented plane waves (APWs) ($RK_{\max} = 7, 8, 9$; more than 220 APWs per atom) and 2000 and 4000 (300 and 637 in the irreducible wedge) k -points in the Brillouin zone were used to obtain converged results. These numbers of APWs for every atom in the unit cell substantially exceed those suggested by Schwarz [26]. The charge densities in the interstitial region were expanded using $G_{\max} = 16$, in contrast to the default value $G_{\max} = 12$. The (L)APW-lo method provides only (velocity/velocity of light)² corrections derived from the Dirac equation for relativistic treatment of valence electrons, and it does not support forces with spin-orbit coupling treated in the second variational step [27]. Hence the calculations of equilibrium volume include velocity mass and Darwin corrections (scalar relativistic mode [25]) to compute the forces and corresponding total energy for each change of volume. The calculations for the FPLO code were done with the local spin density approximation (LSDA) [28] and the generalized gradient Perdew-Burke-Ernzerhof (GGA-PBE) approximation [29], whereas in the (L)APW+lo case also two additional forms, namely GGA-PBESOL [30] and GGA-WC [31], were applied.

To assess the effect of different types of structure compression on exchange coupling, we used the augmented spherical waves method in the GGA, generalized to deal with noncollinear magnetism and spin-orbit coupling (SOC),

applied on U_2Ni_2Sn in Ref. [17], where more details are given.

III. RESULTS AND DISCUSSION

A. Ambient pressure resistivity

The RRR value for the U_2Ni_2Sn single crystal reaches 11 or 12 for the [110] or [001] direction, respectively. It is therefore substantially better than for the polycrystals studied so far. The fact that RRR is practically the same for the current along c and along the basal plane means that U_2Ni_2Sn avoids a superzone boundary effect, i.e., the effect of doubling of a magnetic unit cell along c halving the Brillouin zone. It means that the Fermi surface is not intersected by the new Brillouin zone boundary appearing in the AF state. In the case of such intersection, the impact on electrical conductivity is quite dramatic for U compounds, giving rise to a giant magnetoresistance effect [32]. In any direction along the basal plane, no superzone gap can appear, as the AF coupling is realized only within one crystallographic unit cell. The RRR value for the microdevice is ≈ 4 for both $i//[110]$ and $[001]$.

The $\rho(T)$ dependences at ambient pressure are summarized in Fig. 2. The maximum resistivities reach $\approx 200 \mu\Omega\text{cm}$, which was assumed to be the maximum resistivity for metallic systems by Mott [33]. The bulk samples with a worse defined geometrical factor have higher resistivity for $i//[110]$. However, this is not fully corroborated by the microdevice data. They give a lower absolute value for $i//[110]$ than for $i//[001]$. The difference is likely to be due to the difficult geometry determination for the bulk samples. This Mott limit corresponds vaguely to several conduction electrons per atom experiencing strong scattering, which reduces the mean free path to the interatomic distance. If such a value is reached due to the enhancement of the ρ_0 in strongly disordered systems, the overall temperature dependence flattens, as electron-phonon scattering cannot contribute significantly if the static disorder gives impurity scattering at almost every atomic site [34]. Indeed, U-based systems, which can be classified as broad $5f$ -band materials, do not exceed the Mott limit. One can observe the flattening of $\rho(T)$ with increasing

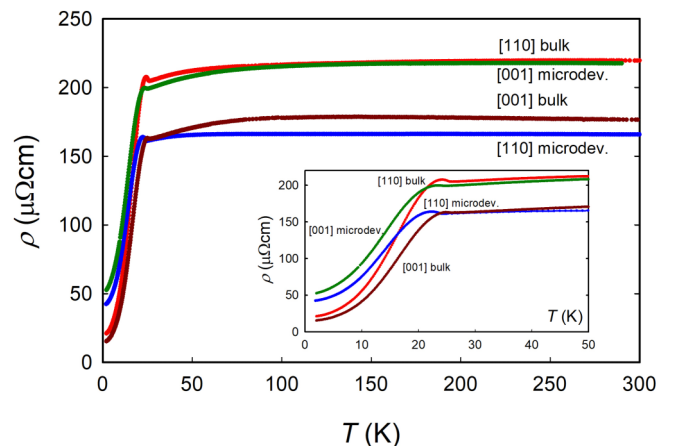


FIG. 2. Temperature dependence of electrical resistivity of the U_2Ni_2Sn single crystal in the form of bulk and microdevice for different current directions.

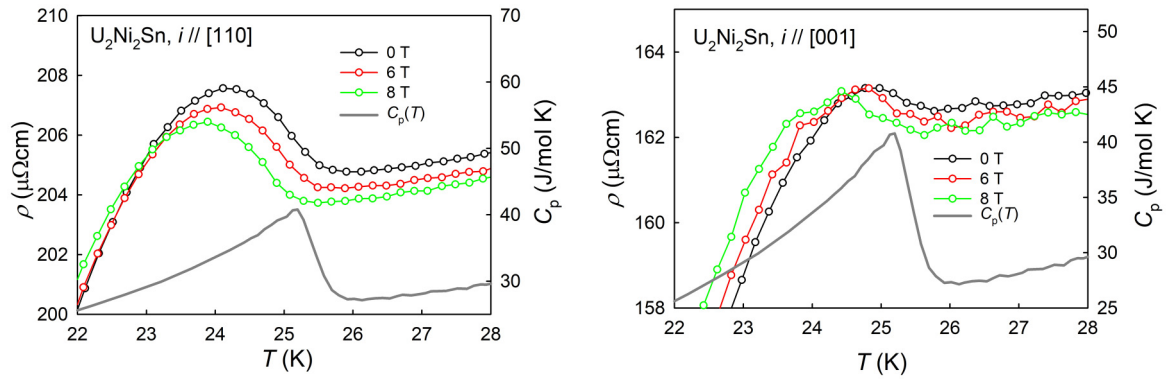


FIG. 3. Temperature dependence of electrical resistivity of U_2Ni_2Sn in the vicinity of the Néel temperature for different current directions in magnetic fields $H//[001]$ up to 8 T.

ρ_0 , e.g., in U-Mo alloys with no magnetic moments on U [35], as well as in UFe_2-UNi_2 Laves phases [36], where the compositions close to the terminal compounds have small U moments ordered ferromagnetically [37]. There are, however, magnetic U systems that have ρ -values significantly exceeding the Mott limit in the paramagnetic state. This feature is evidently not related to atomic disorder or low concentrations of conduction electrons, as they can have very low residual resistivity, so the overall character of $\rho(T)$ remains metallic. One of them is UGa_2 [6], with ρ reaching $300 \mu\Omega \text{ cm}$. From other prominent cases, one can mention antiferromagnets $UNiGa$ [38] or $UNiGe$ [39]. The reason for such high resistivity is arguably the strong scattering on disordered U moments in the paramagnetic state. The relation to disorder is emphasized by the negative resistivity slope, shared with highly disordered alloys [40], and attributed to a weak localization, more specifically to the temperature-induced disruption of coherence of wave functions. Such “dephasing” suppresses the predominant backward scattering of conduction electrons, which takes place if the electron wavelength is comparable with the mean free path λ . In systems with fluctuating moments, the difference is that the electron-phonon scattering, which is inelastic, is superimposed by similarly inelastic scattering on spin fluctuations [40].

U_2Ni_2Sn remains with values reaching $200 \mu\Omega \text{ cm}$ at the conventional upper (Mott) limit. Comparing with polycrystalline data, it is somewhat surprising that the negative slope at high temperature appears as a much weaker effect, seen both for the bulk and microdevice only for $i//[001]$. The decrease for the bulk crystal is from the maximum of $178.5 \mu\Omega \text{ cm}$ at 150 K to $176.5 \mu\Omega \text{ cm}$ at 300 K, i.e., only 1.2%. The decrease reported for the polycrystal was more than 20% [13]. This may indicate that the negative slope develops only in possibly more disordered polycrystals. Naturally, we cannot exclude small variations of stoichiometry. The extended off-stoichiometries reported for U_2Pd_2Sn [41] are, however, most likely missing in the case of U_2Ni_2Sn ; otherwise, identical T_N values would not be obtained in U_2Ni_2Sn produced in different laboratories and by diverse techniques.

Details of the transition are seen in the inset of Fig. 2 and in Fig. 3. It is evident that $\rho(T)$ exhibits a small increase with decreasing T in conjunction with the AF order, and this feature is seen better in the single-crystal data than in previous polycrystal studies [13,14]. One can also recognize

that it is more pronounced for current in the basal plane rather than along [001]. The maximum is the result of an interplay between the tendency for higher resistivity in the AF state and the decrease with further decreasing T due to freezing out of magnetic excitations. The increase cannot be simply attributed to any magnetic superzone boundary effect. If it existed, it would predominantly affect the $i//[001]$ geometry due to the magnetic unit cell doubling along c . The more pronounced effect for $i//[110]$ suggests that more subtle effects related to magnetic order, such as modification of the electronic structure and/or concomitant spontaneous magnetostriction, manifested mainly as the rotation of the square motif of the U atoms in the basal plane [16], may be the driving force. It is instructive to see that modifications of magnetic coupling can dramatically change the situation around the Fermi level (see Fig. 3 in [17]). One can also notice that the $i//[001]$ geometry has the maximum below T_N reduced to a shoulder, while $\rho(T)$ tends to increase above T_N . The increase saturates at 100–150 K and the weak decrease mentioned above follows up to room temperature. The difference with respect to the current in the basal plane case can reflect a different correlation length of magnetic moments above T_N in different directions.

From the details of the transition shown in the inset of Fig. 2 and in Fig. 3 one can notice that the increase starts just below the ordering temperature, marked by the sharp specific-heat anomaly (data from [16]). Figure 3 also gives information on the effect of magnetic field applied along [001], which is the easy-magnetization direction [16]. There is a shift of T_N to lower temperatures following a generic magnetic phase diagram of antiferromagnets [16]. One can also distinguish a small reduction of resistivity in the temperature range above T_N , which can be due to the suppression of magnetic fluctuations affecting mainly the current in the basal plane.

The anomaly in $\rho(T)$ observed for the microdevice exhibits a small (by 2 K) shift toward lower temperatures. A series of careful experiments with different excitation currents proves that this effect is not related to a sample heating. Using different PPMS systems, we also eliminated the possibility that a shift in temperature calibration would be responsible for the misfit. Therefore, we cannot exclude that the FIB treatment modified to some extent the microstructure or introduced strains.

At low temperatures, magnetic field applied along c increases the resistivity for currents in both directions studied.

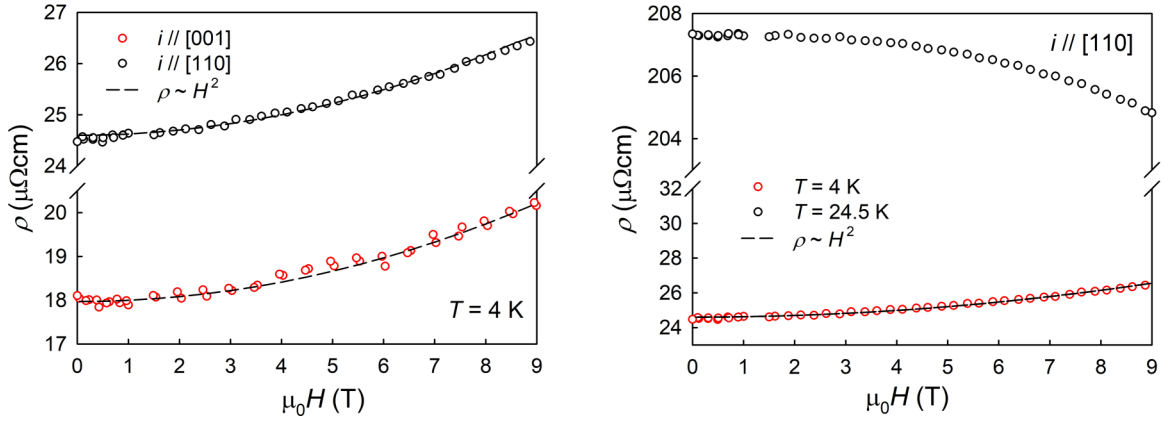


FIG. 4. Field dependence of the resistivity of U_2Ni_2Sn at $T = 4$ K (left) and 24.5 K (right). The current directions are indicated in the legend. The magnetic field was applied along the $[001]$ direction. The dashed lines for both current directions correspond to the $\rho \sim H^2$ fit. Notice the axis breaks.

This is understood to be due to the field effect on the sublattice with magnetization antiparallel to the field, which is destabilized, bringing additional spin fluctuations [42]. As seen from Fig. 4, the field effect is quadratic, with $\rho(H)$ well-described by

$$\rho = \rho_{H=0} + \chi_2 H^2 \quad (1)$$

with $\chi_2 = 0.03 \mu\Omega \text{ cm T}^{-2}$ for $i//[001]$ and $\chi_2 = 0.02 \mu\Omega \text{ cm T}^{-2}$ for $i//[110]$.

On the other hand, magnetoresistance at higher temperatures is negative, reflecting the suppression of fluctuations in the vicinity of T_N by a magnetic field. The crossover temperature of the two tendencies is seen in Fig. 3 as the point where $\rho(T)$ curves in different fields cross. We can deduce that such T_c is lower for $i//[110]$ (23 K) than for $i//[001]$ (24.5 K). The difference is apparently in the higher positive magnetoresistance on the magnetic side of the phase transition for $i//[001]$, which can be associated with the fragility of the AF coupling, deduced from computations of different intersite effective exchange parameters [18].

The behavior of $\rho(T)$ below T_N should reflect the electron-electron scattering (depending on the density of states at the Fermi level, or, in another words, on the electron effective mass), and the scattering of electrons on magnetic excitations. Having a pronounced uniaxial anisotropy, quantified as $E_a/k_B \approx 170$ K [16], where E_a is the anisotropy energy per 1 U atom and k_B is the Boltzmann constant, the presence of low-energy collective magnonlike excitations is unlikely. Indeed, the conventional Fermi liquid power law

$$\rho = \rho_0 + AT^2 \quad (2)$$

is followed up to $T = 7$ K for both current directions. At higher temperatures (Fig. 5) an additional contribution appears, which can be ascribed to an exponential temperature dependence. We parametrized the resistivity using the function

$$\rho = \rho_0 + AT^2 + BT \exp\left(-\frac{\Delta}{T}\right), \quad (3)$$

which provides a reasonable fit up to $T \approx 17$ K, i.e., quite close to T_N . The value of the spin gap Δ should reflect the energy

of flipping of individual U moments, which should be of the order of the ordering temperature. The effect of electron-phonon scattering, weaker compared to the dramatic effect of scattering on magnetic excitations particularly far below the Debye temperature $\Theta_D = 167$ K [16], was neglected here. The actual values of fitting parameters are shown in Table I.

Considering the weighted average of $A = [(A_{001})/3]^2 + (2/3 \times A_{110})^2]^{1/2} = 0.27 \mu\Omega \text{ cm K}^{-2}$, we can use the Kadowaki-Woods relation $A/\gamma^2 \approx 10^{-5} \mu\Omega \text{ cm}/(\text{mJ/mol K}^2)^2$ [43] to check the consistency of the model, i.e., whether the deduced Fermi liquid A is really due to an elevated density of states at the Fermi level. Indeed, using $\gamma = 187$ mJ/mol f.u. K^2 [16], giving 93.5 mJ/mol U K^2 , we obtain $A/\gamma^2 \approx 3 \times 10^{-5} \mu\Omega \text{ cm}/(\text{mJ/mol U K}^2)^2$, which is within an acceptable margin from the model value.

B. High-pressure effect on resistivity

After the ambient pressure experiments, the same samples were loaded into the pressure cell and measured with pres-

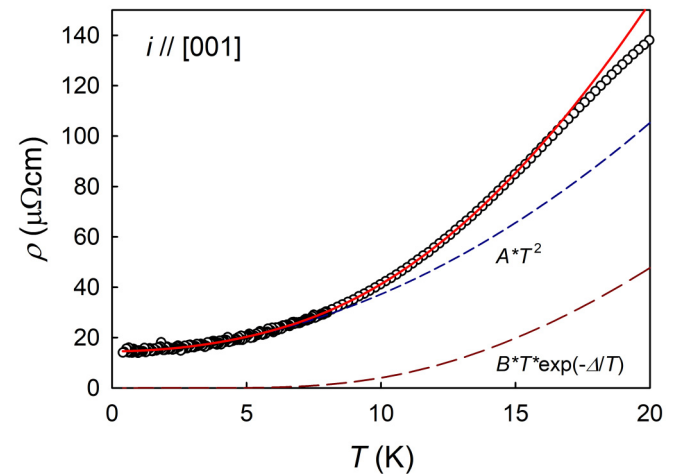


FIG. 5. Temperature dependence of electrical resistivity for $i//[001]$ with the fit to the function (3) (red line), together with its individual components (dashed lines).

TABLE I. Values of the fitting parameters.

	ρ_0 ($\mu\Omega$ cm)	A ($\mu\Omega$ cm K $^{-2}$)	Δ (K)
$i//[001]$	15	0.23	36
$i//[110]$	20	0.29	30

sure increasing in several steps up to 3.3 GPa. The samples were arranged close to the center of the cell and the magnet axis, ensuring the pressure and field homogeneity. The orientation of the samples was kept the same, corresponding to the previous ambient pressure experiment, i.e., the setup allowed simultaneous measurement with current directions along different crystallographic directions, while the magnetic field was applied always along the c -axis.

Figure 6 illustrates the effect of pressure on the electrical resistivity for $i//[001]$. It contains the $\rho(T)$ data only for the selected pressures for better visualization. The remaining curves fall in between the corresponding pressures, but this limited set conveys the main tendencies. One can see that the application of pressure affects mainly the behavior close to the critical temperature. Besides a small shift of ordering temperature, there is a progressive suppression of resistivity in the intermediate temperature range. The part above the transition is well seen from the overview in Fig. 6. The pressure-induced resistivity decrement is reduced when T increases and becomes negligible above $T = 200$ K. The suppression of resistivity in the ordered state can be seen due to the very high slope only in the detailed plot. The detail in Fig. 7 demonstrates that the residual resistivity stays almost invariable. The changes in the resistivity, measured for the current direction $i//[110]$ (not shown here), are very similar.

Such a tendency, which was followed over a very large pressure range, e.g., for UPt_3 [44], is interpreted as a suppression of the spin fluctuation effect, the energy scale of which extends progressively to higher energies and does not interfere with the temperature scale covered by a cryogenic experiment. The lack of low-energy excitations results in the decrease of

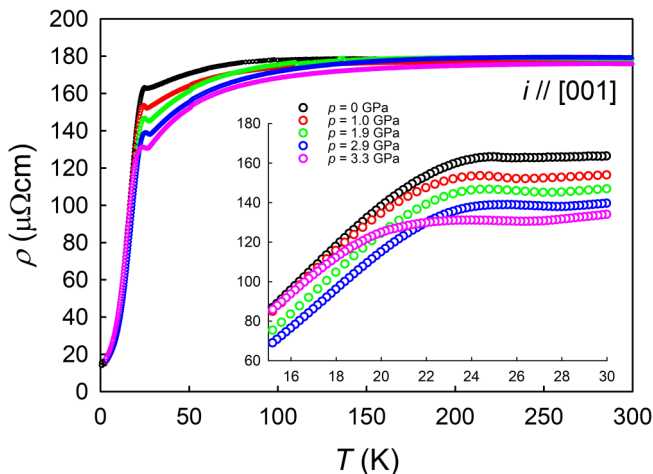


FIG. 6. Pressure effect on the zero-field resistivity of $\text{U}_2\text{Ni}_2\text{Sn}$ for $i//[001]$. The inset shows the vicinity of the inflection point.

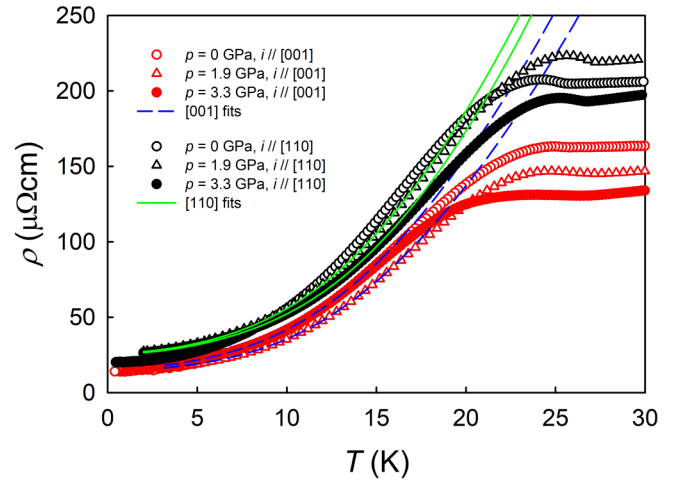


FIG. 7. Temperature dependence of electrical resistivity $\rho(T)$ in selected pressures for the two current directions. The lower curves correspond to $i//[001]$, the upper ones to $i//[110]$. The solid lines represent the result of the curve fitting by Eq. (2).

the quadratic coefficient A , i.e., of the Sommerfeld coefficient γ via the Kadowaki-Woods relation.

It is also instrumental to compare $\text{U}_2\text{Ni}_2\text{Sn}$ with similar high-pressure data on uranium ternary UCoAl [45]. This compound does not have long-range magnetic order, but ferromagnetism can be simply introduced by very small doping of, e.g., Fe. This, however, adds only a cusp at T_C to otherwise invariable $\rho(T)$. Thus, one can realize that the large-scale resistivity features have in fact very little dependence on magnetic order. For $\text{U}_2\text{Ni}_2\text{Sn}$ this means that one can attribute the reduction in resistivity below $T \approx 150$ K to a gradual suppression of the size of individual fluctuating magnetic moments.

A detailed quantitative analysis of the low-temperature part can be done using formula (3) even at elevated pressures. The results shown in Fig. 8 indicate systematic variation for all refined variables, except perhaps the last point at 3.3 GPa, i.e., the pressure exceeding the nominal maximum of the given pressure cell. The reduction of A to $\approx 50\%$ of the zero-pressure value means a reduction of γ to $\approx 70\%$. The residual resistivities increase slightly. The width of the spin gap Δ increases as well for both current directions.

The inflection point, which is used to track the transition temperature, is affected by a magnetic field very similarly to the ambient pressure case. It is displaced toward lower temperatures by the increasing field at any given pressure. Hence, the ordering in $\text{U}_2\text{Ni}_2\text{Sn}$ remains antiferromagnetic up to the highest achieved pressure of 3.3 GPa. The magnetoresistance measurements at elevated pressures support this conclusion: the $\rho(H)$ curves are parabolic at low temperatures and become weakly decreasing just above the temperature of the inflection point (not shown here), as expected for the antiferromagnets around the Néel temperature [42]. The prefactors χ_2 in the $\chi_2 H^2$ term of Eq. (1) are affected by pressure: for $i//[001]$ the χ_2 decreases from 0.03 to $0.02 \mu\Omega$ cm T^{-2} , and for $i//[110]$ the χ_2 increases from 0.02 to $0.04 \mu\Omega$ cm T^{-2} .

The most interesting process is the change of the Néel temperature with pressure. As seen in Fig. 3, the antiferromagnetic phase transition can be associated with the beginning

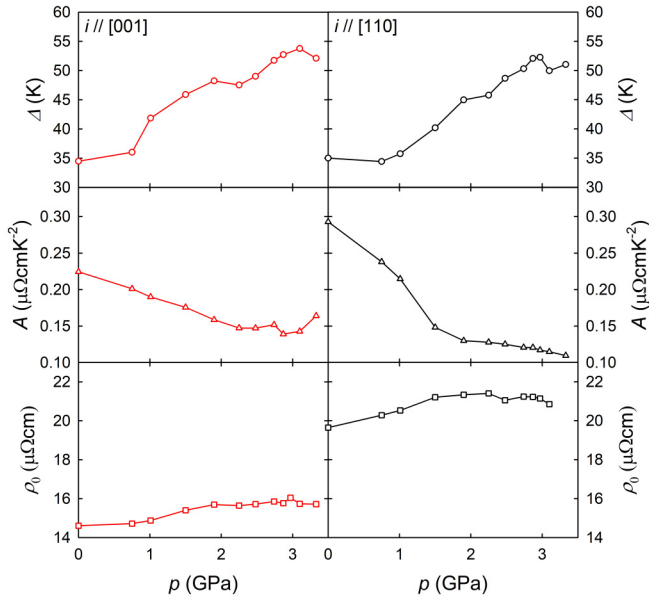


FIG. 8. Pressure dependence of parameters (ρ_0 , A , and Δ) used to fit the temperature dependence of resistivity of $\text{U}_2\text{Ni}_2\text{Sn}$ at various pressures. The lines in the graphs are the eye-guides.

of the upturn. This point is, however, not very well-defined, and we decided to track the inflection point, which is typically 0.5 K below T_N , but it can be determined more precisely using the derivative $d\rho(T)/dT$. The Néel temperature, determined in this way, increases with increasing pressure until 2.9 GPa (Fig. 9) and then starts to decrease. Such behavior has been observed for both current directions.

The initial increase can be quantified as $dT_N/dp = 0.6$ K/GPa, or $d(T_N/dp)/T_N = d \ln T_N/dp \approx 0.024$ GPa^{-1} . The latter value is comparable with UAs ($d \ln T_N/dp = 0.02$ GPa^{-1} [46]), which, however, has much higher $T_N = 127$ K. UGa_2 with $T_C = 126$ K has $d \ln T_N/dp = 0.032$ GPa^{-1} , as deduced from data in Ref. [6]. Even more meaningful is a parameter relating the changes of T_N to the change of volume, considering the bulk modulus of the compound. This, however, was not known for $\text{U}_2\text{Ni}_2\text{Sn}$. Therefore, we undertook a structural study using XRD under pressure, which should also determine the stability of the structure, i.e., whether a structural phase transition appears in the pressure range where resistivities were studied, and whether the sudden downturn of T_N at 3 GPa is primarily the structural effect.

The pressure variations of ordering temperature close to the thermodynamic equilibrium should follow the well-known Ehrenfest relation for the second-order phase transition:

$$dT_N/dp = 3\Delta\alpha V T_N / \Delta C_p, \quad (4)$$

where $\Delta\alpha$ is the difference between the linear thermal expansion coefficients below and above the transition, V is the molar volume (5.81×10^{-5} m^3 at $T = 26$ K), and ΔC_p is the height of the step of specific heat at the transition (-15.3 J/mol K [16]). There are no dilatometry data available for $\text{U}_2\text{Ni}_2\text{Sn}$, and the x-ray diffraction data in [16] do not have enough resolution to distinguish relatively weak spontaneous magnetostriction effects, which can give an estimate of the

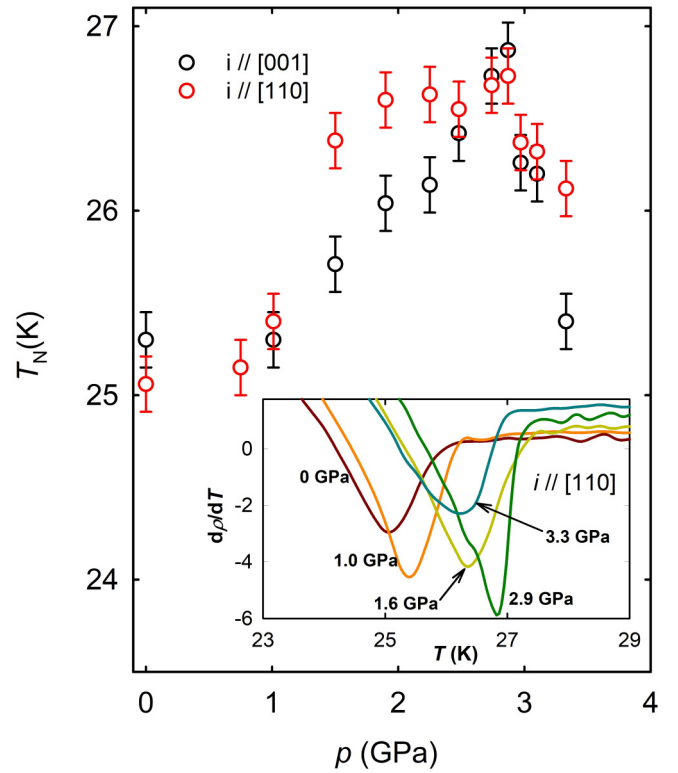


FIG. 9. Pressure dependence of the Néel temperature of $\text{U}_2\text{Ni}_2\text{Sn}$ derived from the zero-field resistivity. The inset shows the temperature dependence of the $d\rho/dT$ derivatives at the selected pressures for $i//[110]$ in the vicinity of the ordering temperature of $\text{U}_2\text{Ni}_2\text{Sn}$. The minima on these derivatives have been used for tracking the $T_N(p)$ dependence.

thermal expansion parameters below and above the transition. However, more detailed data displayed in Ref. [47] indicate that there is approximately a compensating c -parameter increase in the AF state, and the a -parameter decreases. Using the data in [47], we attempted to estimate individual thermal expansion parameters for both parameters and their change at the transition. The change of α_a , $\Delta\alpha_a \approx -5.2 \times 10^{-5}$ K^{-1} , and the change of α_c , $\Delta\alpha_c \approx +11.2 \times 10^{-5}$ K^{-1} , give the positive volume effect $2 \times \Delta\alpha_a + \Delta\alpha_c$ [replacing $3\Delta\alpha$ in (4)] $= 0.8 \times 10^{-5}$ K^{-1} . The resulting dT_N/dp comes out weakly negative, and, using the parameters given here, we obtain $dT_N/dp \approx -0.8$ K/GPa. However, considering the large uncertainty in the determination of the thermal expansion around T_N , we can conclude that the expected thermodynamic effect is close to zero, and $dT_N/dp = 0.6$ K/GPa is not in contradiction with other observable quantities.

C. High-pressure structure study

We collected x-ray diffraction data at pressures up to 18 GPa at room temperature. The diffraction patterns exhibit a continuous pressure development, indicating no major structure modification taking place in this pressure range. However, more detailed inspection reveals additional peaks, which may originate from splitting due to a reduction in symmetry. Such splitting develops smoothly with pressure (Figs. 10 and 11), pointing indeed to a reduced symmetry of the crystal lattice.

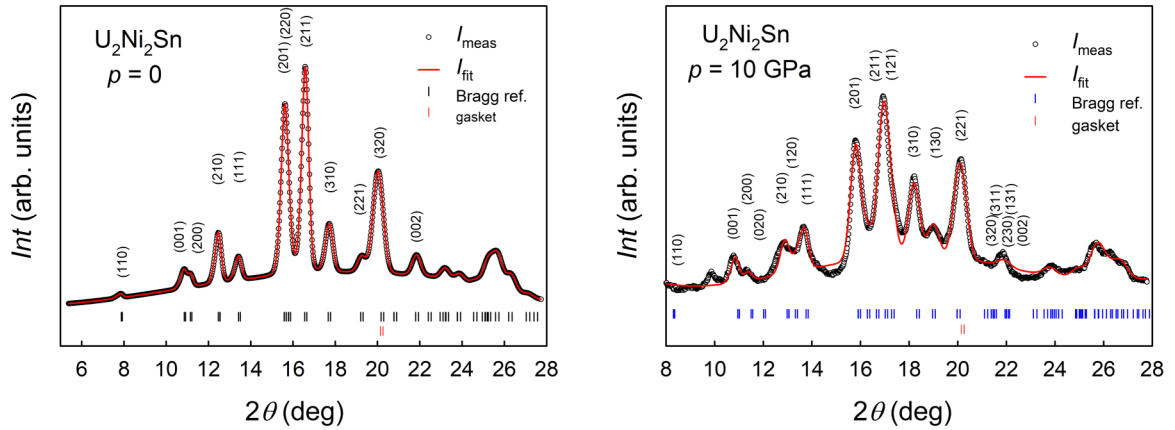


FIG. 10. XRD patterns of U_2Ni_2Sn taken at zero pressure (left) and at 10 GPa (right) using Mo radiation. The red line represents the fit. The peak positions are marked by the ticks at the baseline. The red ticks indicate the positions of lines belonging to the gasket.

Revisiting possible structure changes due to H absorption, we found a striking similarity with $Nd_2Ni_2SnH_6$, in which hydrogen absorption induces an orthorhombic distortion, lifting the equivalence of the a - and b -axis, and giving the space group $Pbam$ [48]. The distortion becomes well visible for pressures $p > 12$ GPa, but it can be traced back to lower pressures, and it is detectable already at $p = 5.3$ GPa. No sign of it exists at $p = 3$ GPa. As we saw that antiferromagnetism of U_2Ni_2Sn undergoes a rapid downturn just above the latter pressure, we suggest that the structure collapses into the orthorhombic phase in the range 3.0–3.5 GPa. As the pressure variation of b does not extrapolate to the same point as a , we speculate that the transition is of the first-order type, and the volume collapse can be estimated as 7% (see Fig. 12). The data exhibit anisotropic elastic properties, and it is evident that the hydrostatic pressure leads to a higher compression of a and b than for the c -axis. This applies already in the low-pressure phase. The striking anisotropy can be related to the anisotropic contribution of $5f$ states to bonding, which was explored in several structure types of equiatomic uranium ternaries [49].

The distorted structure gives the lattice parameter b about 4% lower than a at $p = 5.3$ GPa, and the difference increases with increasing p . In addition, the transition is accompanied by a certain drop of c . The linear compressibilities can be evaluated as $k_a = 1.12 \times 10^{-3} \text{ GPa}^{-1}$, $k_b = 2.46 \times 10^{-3} \text{ GPa}^{-1}$, and $k_c = 0.82 \times 10^{-3} \text{ GPa}^{-1}$, giving the volume compressibility $k_V = k_a + k_b + k_c = 4.26 \times 10^{-3} \text{ GPa}^{-1}$. The corresponding bulk modulus in the high-pressure phase is $B = (235 \pm 5) \text{ GPa}$. The lattice of the tetragonal phase is softer, and one can estimate $k_a = 6.3 \times 10^{-3} \text{ GPa}^{-1}$ and $B = (80 \pm 10) \text{ GPa}$ if we assume $k_c \approx 0$. If we calculate the unit cell volume at each pressure point of the tetragonal phase and plot it as a function of p , we obtain $k_V = 9.6 \times 10^{-3} \text{ GPa}^{-1}$ and $B = (104 \pm 5) \text{ GPa}$.

To compare with other U_2T_2X compounds, high-pressure structure data exist for U_2Pt_2In , which has a very similar structure type [50]. The linear compressibilities $k_a = 2.20 \times 10^{-3} \text{ GPa}^{-1}$ and $k_c = 2.42 \times 10^{-3} \text{ GPa}^{-1}$ have opposite but much smaller anisotropy. This agrees with the fact that the short U-U spacings within the basal plane indicate it as the strong $5f$ bonding direction, which is not the case in U_2Pt_2In . The bulk modulus of U_2Pt_2In , deduced from the data in [50], $B = 147 \text{ GPa}$, is higher than for the low-pressure phase of U_2Ni_2Sn . Among magnetic systems, the pressure variations of T_N were investigated for U_2Pd_2In , revealing a decreasing tendency from $T_N = 37.4 \text{ K}$ at $p = 0.2 \text{ GPa}$ to 35.2 K at 1.8 GPa [50]. However, no structure data for the high-pressure state are available.

Knowledge of the bulk modulus of U_2Ni_2Sn ($B = 80 \text{ GPa}$ in the tetragonal phase) allows us to determine the relative volume sensitivity of T_N , $d \ln T_N / d \ln V = -2.6$, comparable, e.g., with the data deduced for UAs (-2.0) in [51].

D. First-principles calculations

First-principles calculations were used for better understanding of the observed phenomena, especially of the mutual relation of structure and magnetism. We performed calculations in a non-spin-polarized state and in a simplified ferromagnetic structure, which could address the bonding conditions and the reaction of magnetic moments to the structure distortion. Another type of calculation, which allowed us

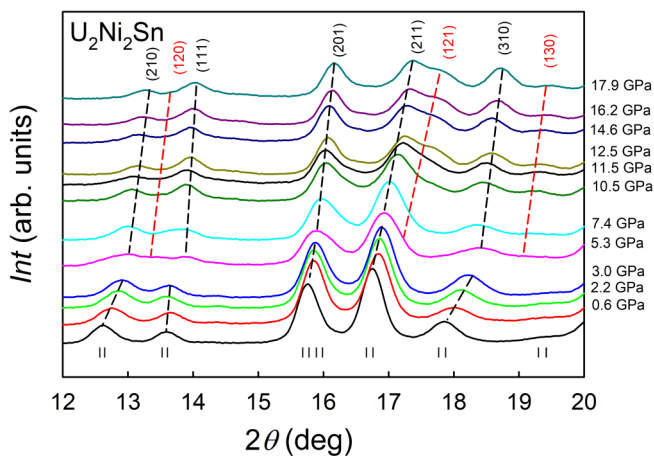


FIG. 11. Pressure variations of XRD patterns of U_2Ni_2Sn (Mo radiation). The black dashed lines mark the peaks of the tetragonal structure. The red dashed lines represent the pressure dependence of the additional peaks originating from splitting due to a reduction of symmetry.

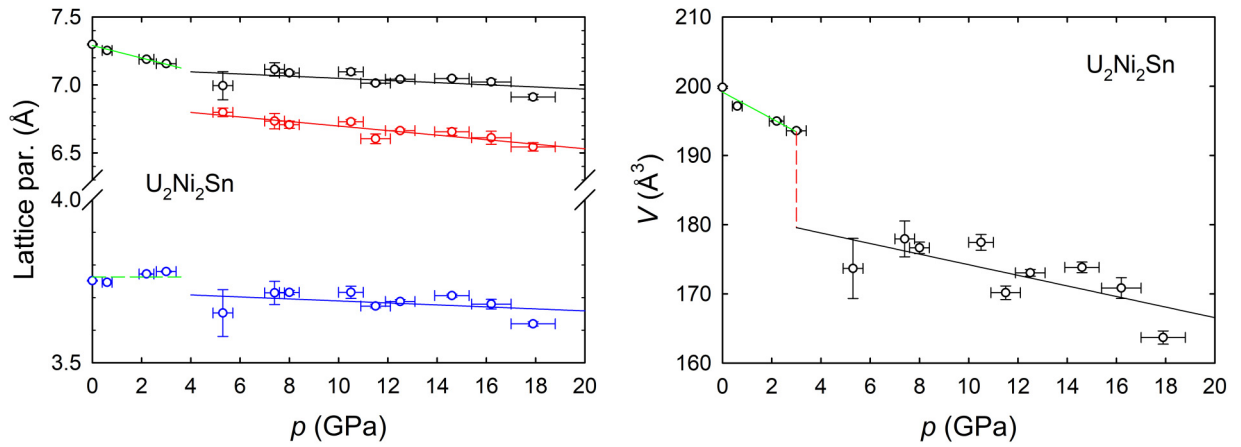


FIG. 12. Pressure dependence of lattice parameters and unit cell volume of U_2Ni_2Sn at room temperature. The lines represent linear fits used to determine the linear and bulk compressibilities mentioned in the text.

to assess different types of exchange coupling and magnetic structures, was used to gain insight into the lattice compression in the absence of distortion.

First, we targeted the high-pressure orthorhombically distorted structure to test its proclivity to the loss of magnetism. As the high-pressure XRD data give reliably only the lattice parameters a , b , and c , but not the internal parameters of U atoms, which are crucial for determining the U-U distances in the ab -plane, we took the values of lattice parameters at a pressure of 8 GPa and relaxed atomic positions using fast and flexible scalar relativistic FPLO calculations with a local-spin-density approximation (LSDA) functional assuming a ferromagnetic state. As the starting parameters, we took those of $Nd_2Ni_2InH_6$ ($Pbam$), where a similar orthorhombic distortion takes place due to the H absorption in Nd_2Ni_2In [48]. The Nd positions $x_{Nd} = 0.68$ and $y_{Nd} = 0.17$ converged for U_2Ni_2Sn to $x_U = 0.6406$ and $y_U = 0.1321$ (see Fig. 13).

The shortest U-U distance, $d_{U-U} = 2.69 \text{ \AA}$, which is within the dimers and is marked by thick black lines, shrinks dramatically from the ambient-pressure value 3.575 \AA [17]. Such impact of pressure may be seen in a broader context of the systematics of U compounds, showing that the closer together

the U atoms are in a given direction, the better they can be additionally compressed together by applied hydrostatic pressure [49]. Such paradox, which can work only if we assume the existence of the soft U-U bonds into which the $5f$ charge concentrates, was deduced earlier for anisotropic variations of lattice parameters. Here in the case of U_2Ni_2Sn , where already the a - c anisotropy follows the above-mentioned rule, there is the additional step using the degree of freedom given by the individual U coordinates not confined by symmetry.

The variations of electronic structure between the ambient- and high-pressure phase can be assessed based on the non-spin-polarized DOS of both phases seen in Fig. 14, obtained by fully relativistic FPLO calculations. One can distinguish the U- $5f$ states, forming a band $\approx 3 \text{ eV}$ wide, with 1 eV below the Fermi level E_F , and 2 eV remaining empty. There is only a very little overlap with the Ni- $3d$ band, occupying the energy range 2–4 eV below E_F . Their mutual hybridization can be seen in the tail of the $3d$ states above E_F and of the $5f$ states at 2.5 eV below E_F . The high-pressure phase exhibits a significant broadening of the $5f$ band. The total width is naturally affected by the spin-orbit splitting between the $5f_{5/2}$ and $5f_{7/2}$ states being 1 eV, which is more visible

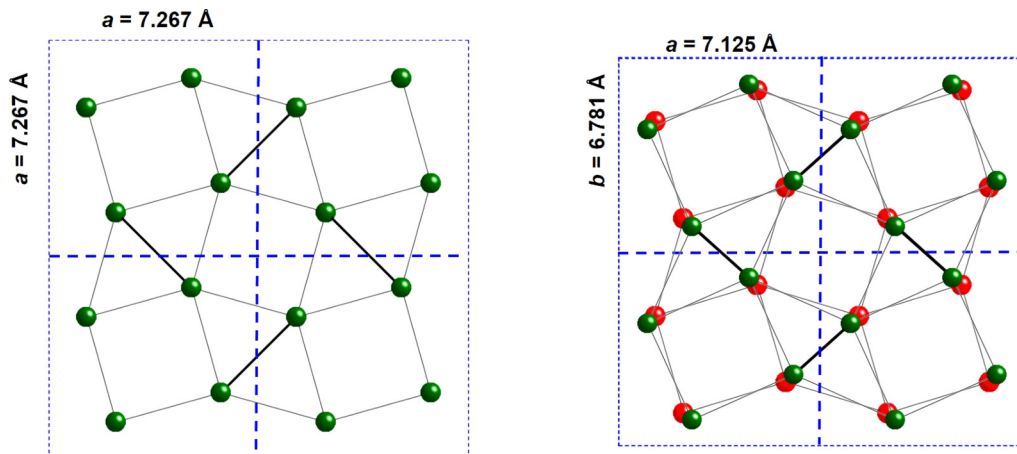


FIG. 13. Comparison of the ground-state crystal structure of U_2Ni_2Sn (left) with the orthorhombic structure at $p = 8 \text{ GPa}$ (right). The U-positions were first taken from $Nd_2Ni_2InH_6$ (red) and then relaxed in LSDA calculations, giving the equilibrium U-position (green).

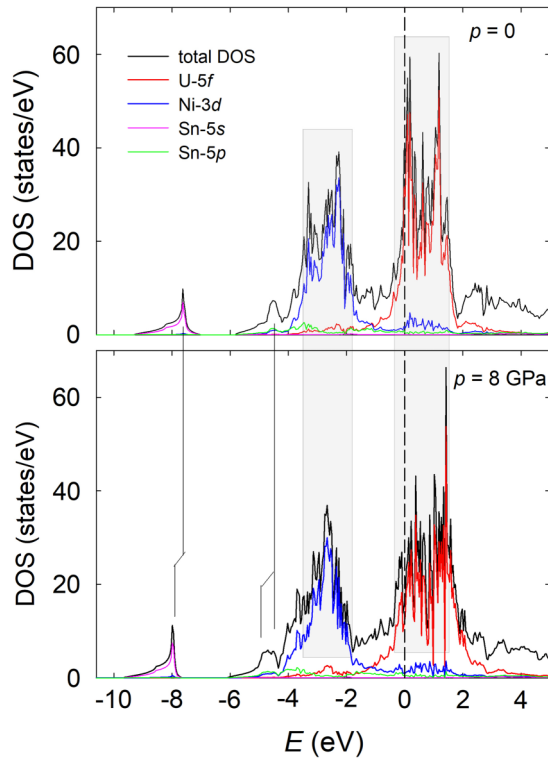


FIG. 14. Variations of the electronic structure of $\text{UNi}_2\text{Ni}_2\text{Sn}$ at ambient pressure and $p = 8$ GPa, the latter with the orthorhombic distortion, obtained in fully relativistic non-spin-polarized calculations. For details, see the full text.

for the ambient pressure phase. The high-pressure phase has individual subbands that are wider and with more pronounced van Hove singularities, which is seen as suppression of the pseudogap, and developing more extended shoulders, especially the one at higher energies (≈ 2 eV above E_F). As a result, the density of states $N(E)$ tends to decrease, which impacts also its value at the Fermi level, $N(E_F)$, being reduced by more than a factor of 2, from 40 to 15 states/(eV unit cell). A certain smaller broadening can be seen also for the $3d$ band. Below the $3d$ band, there is a smaller but interesting feature at 4.5 eV binding energy, which has no $5f$ states, but comprises some $3d$ states of Ni, the s and p states of Sn, $6d$ states of U, as well as Ni- $4s$ states (both latter ones not shown individually here). This feature can hence be denoted as a hybridization peak. Consequently, it gets significantly widened in the high-pressure phase. The predominantly Sn- $5s$ peak shifts from 7.6 to 8.0 eV binding energy in the high-pressure phase. Occupancies of individual states change to some extent as well. The $5f$ occupancy $n_{5f} = 2.72$ in the ambient pressure phase increases to 2.77 in 8 GPa, while n_{6d} increases from 2.02 to 2.20. The Ni $3d$ state population $n_{3d} = 8.72$ remains rather invariable. The total U ion charge $+0.72|e|$ is reduced to $+0.64|e|$. The polarity of the bonds is illustrated by the electron excess (negative charge) on Ni $-0.54|e|$ ($-0.52|e|$ at 8 GPa) and on Sn $-0.35|e|$ ($-0.23|e|$ at 8 GPa).

The short U-U distances in the high-pressure phase, which are far below the Hill limit 3.4 \AA [52], can be naturally detrimental for magnetism of $\text{U}_2\text{Ni}_2\text{Sn}$ even if the multiplicity of the nearest neighbors is low. We tried to get more information

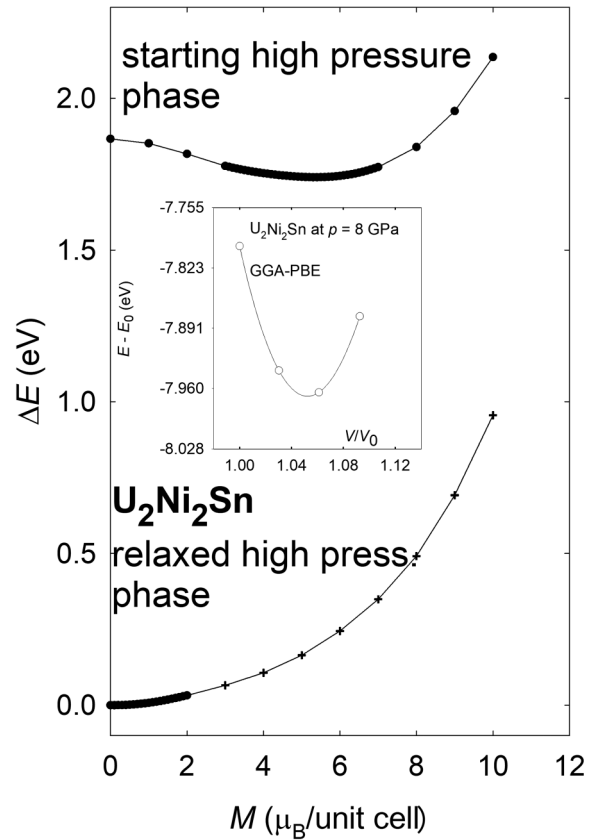


FIG. 15. Increase of total energy if a magnetic moment is prescribed in the high-pressure phase of $\text{U}_2\text{Ni}_2\text{Sn}$ —comparison of the starting and relaxed phase from Fig. 13. The inset shows the energy vs volume dependence for the high-pressure phase obtained using the GGA-PBE calculations. V_0 is the experimental equilibrium volume. E_0 was set arbitrarily.

on the fate of magnetism upon the orthorhombic distortion using the same computational method. At first, we identified that the ground state is indeed paramagnetic in the compressed orthorhombic phase. The stability of the paramagnetic state is demonstrated by means of the fixed spin moment method using scalar relativistic FPLO. Such an approach is based on variations of the total energy when a fixed spin moment is assumed, taking for simplicity the order as ferromagnetic. The calculated curve has a clear minimum at zero magnetic moment of the orthorhombic unit cell (see Fig. 15). The magnetic moment was first varied in steps of $0.1 \mu_B$. As the increase of total energy has a progressive tendency, the step was later increased to $1 \mu_B$ and the dependence was followed up to $10 \mu_B$, which corresponds to the magnetic moment $M = 2.25 \mu_B$ on 1 uranium atom. The comparison with the orthorhombically distorted structure used as a starting point for relaxation of atomic positions, which has somewhat larger $d_{\text{U-U}} = 3.449 \text{ \AA}$ and develops U spin moments of $1.2\text{--}1.3 \mu_B$, reveals that the extreme shrinking of the distance with the U-U dimers is responsible for the loss of magnetism in the high-pressure phase.

The basic test of whether the computations are based on a solid foundation is a comparison of the calculated equilibrium volume with the experimental one. We reached a very good

agreement using the WIEN2K package with the GGA-PBE approximation, giving the V_0 value within 0.1% from the experimental one for the ambient pressure tetragonal phase. The fact that the DFT+ U method does not have to be applied implies that U_2Ni_2Sn is essentially a $5f$ -band system without electron-electron correlations dominating the energy scale. The obtained bulk modulus $B = 109$ GPa (calculated assuming homogeneous volume variations) is also close to the experimental value obtained in the high-pressure structure study for the tetragonal structure. The calculated bulk modulus corresponding to the orthorhombic structure at $p = 8$ GPa comes out higher, namely $B = 156$ GPa, which can only be partly explained by renormalizing the volume itself, which decreases from 200.0 to 176.2 \AA^3 at $p = 8$ GPa, i.e., by 12% only. The real bulk modulus of the orthorhombic phase is still substantially higher.

The performance of the LSDA and GGA methods can be compared with respect to the volume of the U_2Ni_2Sn orthorhombic phase. We have calculated the variation of non-spin-polarized total energy with respect to V/V_0 (V_0 is the experimental volume at $p = 8$ GPa). In each iteration step, we computed forces and checked that they are small. The LSDA [28] value comes out 2.34% smaller than V_0 . This is the typical deviation (overbinding) obtained in LSDA full-potential calculations. The GGA-WC and GGA-PBESOL results of V/V_0 are, respectively, 0.69% larger and 0.06% smaller. The frequently used GGA-PBE method gives V_0 4.5% higher than the experimental value at 8 GPa (see the inset in Fig. 15), while it gave the correct V_0 for the tetragonal phase [17]. Computational probing of the high-pressure structure in the simplest approach can be taken as exposing a hypothetical orthorhombic structure with the volume 182 \AA^3 , obtained by extrapolation to $p = 0$, to a pressure (8 GPa) induced compression, which in our case amounts to $\approx 3.5\%$ lower volume. Such construction can bring the GGA-PBE results close to reality. We have eventually included also spin-orbit coupling (SOC) in the second-order variational step [27], but it has only a small influence on the volume. A brief comparison of the enthalpies of both phases indeed gives more stable orthorhombic structure at elevated pressures. The crossover appears at $p \approx 2$ GPa in such calculations, which, however, suggests that the tetragonal structure type may again become stable for $p > 36$ GPa, provided the internal parameters of the structure and the c/a ratio maintain their ambient pressure value, and the orthorhombic structure carries the internal parameters refined for $p = 8$ GPa. The uniaxial magnetic anisotropy with the easy magnetization direction along the c -axis was reproduced by the same type of calculation assuming a ferromagnetic state. A larger orbital $M_L = 1.68 \mu_B$ and smaller and antiparallel spin moments $M_S = -1.59 \mu_B$ per U atom are accompanied by small induced spin and orbital magnetic moment of nickel, $\approx 0.11 \mu_B$ and $0.03 \mu_B$, respectively. Spin and orbital magnetic moments of tin are smaller than $0.05 \mu_B$. The magnetization comes out unrealistically small compared to experimental moments (in the antiferromagnetic state) of $0.88 \mu_B/U$ [16], but one has to bear in mind that the total moment is in any case a small difference of the larger orbital and spin components. The calculated energy of magnetocrystalline anisotropy is

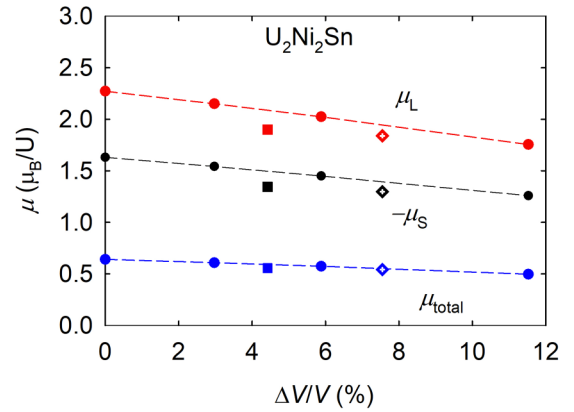


FIG. 16. Volume variations of the spin, orbital, and total magnetic moments of U_2Ni_2Sn . The circles represent the case of isotropic compression, the squares show compression only in a , and the diamonds show additional small c -axis compression. For the latter two cases, the a -axis compression corresponds to the low-pressure tetragonal phase extrapolated to high pressures of $p \approx 14$ GPa, chosen to make the tendencies more pronounced.

equal to 0.81 mRy/U, close to the experimental value of 1.07 mRy [16].

A more detailed study of the volume dependence of magnetism was performed by means of the augmented spherical wave (ASW) method generalized to deal with noncollinear magnetism and spin-orbit coupling. This method, using the GGA, was found to reproduce correctly the antiferromagnetic structure of U_2Ni_2Sn [17] including strong uniaxial anisotropy with the c -axis as the easy-magnetization direction. In the context of the high-pressure study, we performed several calculations with reduced lattice volumes. For simplicity, we maintained the tetragonal symmetry and internal structure parameters of the ambient pressure phase. First, the calculations were performed for lattices uniformly compressed along all crystallographic axes by 1%, 2%, and 4%. As the structure study indicated a higher compressibility for the a -direction, we reduced only a by 4%, maintaining the value of c . In the third type of calculation, the a -parameter from the second type of calculation is combined with c reduced by 1%. This set of calculations should allow us to reveal the tendencies in the variation of the physical quantities caused by the reduction of individual lattice parameters.

There are several interesting tendencies seen from Figs. 16 and 17, summarizing the results. Although the total magnetic moments decrease weakly and linearly as a function of reduced volume, and the possible anisotropy of the compression seems irrelevant, individual spin and orbital moments are much more sensitive, especially if the compression is predominantly realized in the a -direction. The drop in orbital moments is projected in the decrease of uniaxial magnetocrystalline anisotropy, which is somewhat higher (in the ground state) than the value given above. The predominant a -axis compression leads also to the decrease of the energy of the ferromagnetic state, which becomes eventually energetically favorable over the antiferromagnetic state AMF-G (using the notation of Ref. [17]). Comparison with the energies for the

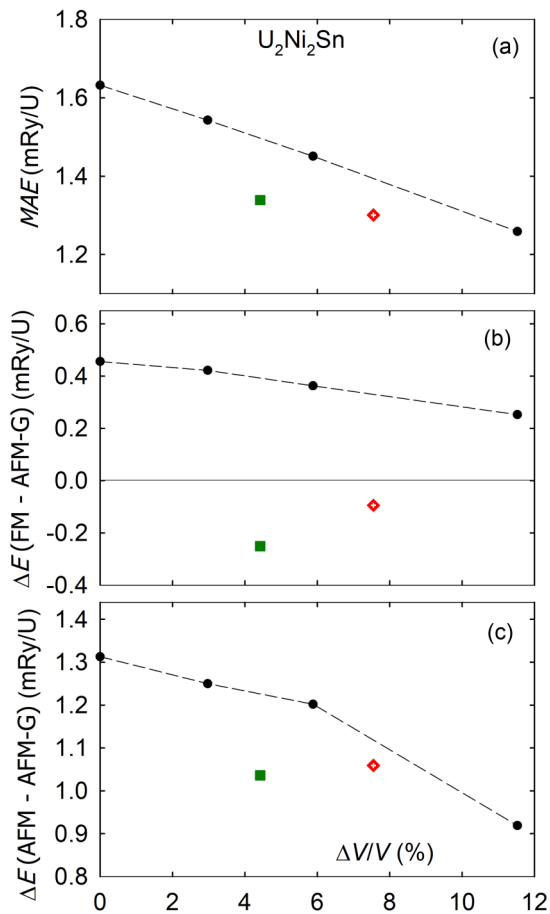


FIG. 17. (a) Variations of magnetic anisotropy energy for the same types of lattice compression as given in Fig. 16. (b) Related energy differences between AFM-G and FM structures. (c) Energy difference between AFM-A and AFM-G structures. AFM-A corresponds to the ferromagnetic coupling of U moments along the c -axis and $+ - + -$ coupling within one unit cell. The decrease of spin moments for high pressures means inexorably also a drop of critical temperatures of magnetic ordering. The increase of T_N , observed at lower pressures, cannot be directly confronted with calculations. In reality, the reduced moments can be over a limited compression range compensated by enhanced effective intersite exchange coupling.

AFM-A structure reveals that the ferromagnetic coupling developing within the basal plane drives U_2Ni_2Sn eventually to the ferromagnetic state, and the ferromagnetic coupling along c causes the energy to increase. However, the collapse of magnetism due to the structural distortion prevents manifestation of the tendency toward ferromagnetism.

IV. CONCLUDING REMARKS

The Néel temperature of U_2Ni_2Sn exhibits as a function of hydrostatic pressure an initial increase from 25 to 27 K. The more compressible lattice in the basal plane, where the nearest U-U neighbors are located, indicates that tuning of the U-U exchange coupling within the plane is important. Exceeding a pressure of 3 GPa, the increasing tendency changes into a

dramatic decrease, which can be related to an orthorhombic distortion of the crystal lattice, bringing the nearest U atoms in the ab -plane very close together. The calculations illustrate that the consequent loss of magnetism is primarily due to the 5f-band broadening. The pressure variations of magnetism could be computed for the nondistorted phase extrapolating from the low-pressure state. They show a decrease of spin and orbital moments, of the magnetocrystalline anisotropy (which remains uniaxial), and a crossover to the ferromagnetic state. The destabilization of U moments is seen in the temperature dependence of electrical resistivity.

The results indicate that long-range magnetism in U_2Ni_2Sn will be lost above $p = 3.3$ GPa. The presence of a quantum critical point is questionable; a first-order transition driven by structural distortion is an alternative scenario. The pronounced pressure sensitivity of T_N and generally of the 5f magnetism in U_2Ni_2Sn can be related to the “soft” U-U dimer bonds, which eventually yield, bringing an orthorhombic distortion with extremely short nearest U-U distances. The fact that the soft structure parameter is also crucial for the magnetic state makes U_2Ni_2Sn and most likely other compounds with the same structure type excellent examples of the tunability of 5f magnetism. More specifically, we observe in the case of U_2Ni_2Sn a typical situation in which the strongest exchange coupling (in our case the ferromagnetic coupling within the U-U dimers) is very sensitive to the distance variations. The fact that very short U-U distances lead to the suppression of magnetism is emphasized in U_2Ni_2Sn by the fact that the distances do not simply scale with the lattice parameters, rather they depend on the internal parameters of U atoms. In other words, the general compression of the structure is supplemented by the rotation of the square motifs of U atoms and ultimately to their deformation. The more compressible a parameter (compared with c) in combination with the “soft” internal parameters of U atoms is the factor that contributes decisively to the pressure variations of magnetic properties.

Aside from the structural distortion, the computations reveal a weakly decreasing trend of U moments with increasing pressure. The individual spin and orbital moments are reduced relatively more. The large reduction of the orbital moments projects into a similar decrease of the uniaxial magnetic anisotropy. The exchange coupling parameters tend to change sign, and in the absence of the structural distortion, ferromagnetism would be established at high pressures.

This type of study underlines the general importance of knowledge of crystal structure variations for high-pressure studies. If the observed development of magnetism were only related to pressure as an external variable, a large part of the physics would be omitted.

ACKNOWLEDGMENTS

This work was supported by the Czech Science Foundation (GACR) under Grant No. 18-02344S. Part of the experiments were performed at MGML [53], which is supported within the program of Czech Research Infrastructures (project no. LM2018096). Also, the support of the Grant Agency of Charles University (GA UK) under Grant No. 814120 is acknowledged.

- [1] J. Lee, M. Matsuda, J. A. Mydosh, I. Zaliznyak, A. I. Kolesnikov, S. Süllow, J. P. C. Ruff, and G. E. Granroth, The Dual Nature of Magnetism in a Uranium Heavy Fermion System, *Phys. Rev. Lett.* **121**, 057201 (2018).
- [2] G. Zwirknagl and P. Fulde, The dual nature of 5f electrons and the origin of heavy fermions in U compounds, *J. Phys.: Condens. Matter* **15**, S1911 (2003).
- [3] S. Ran, C. Eckberg, Q.-P. Ding, Y. Furukawa, T. Metz, S. R. Saha, I.-L. Liu, M. Zic, H. Kim, J. Paglione, and N. P. Butch, Nearly ferromagnetic spin-triplet superconductivity, *Science* **365**, 684 (2019).
- [4] H. von Löhneysen, F. Huster, S. Mock, A. Neubert, T. Pietrus, M. Sieck, O. Stockert, and M. Waffenschmidt, Non-Fermi-liquid behavior in strongly correlated electron systems, *Physica B* **230-232**, 550 (1997).
- [5] A. L. Cornelius, J. S. Schilling, O. Vogt, K. Mattenberger, and U. Benedict, High-pressure susceptibility studies on the ferromagnetic uranium monochalcogenides US, USe and UTe, *J. Magn. Magn. Mater.* **161**, 169 (1996).
- [6] A. V. Kolomiets, J.-C. Griveau, J. Prchal, A. V. Andreev, and L. Havela, Variations of magnetic properties of UGa₂ under pressure, *Phys. Rev. B* **91**, 064405 (2015).
- [7] M. N. Peron, Y. Kergadallan, J. Rebizant, D. Meyer, S. Zwirner, L. Havela, H. Nakotte, J. C. Spirlet, G. M. Kalvius, E. Colineau, J. L. Oddou, C. Jeandey, J. P. Sanchez, and J. M. Winand, A new family of actinide ternary intermetallic compounds, *J. Alloys Compd.* **201**, 203 (1993).
- [8] F. Mirambet, B. Chevalier, L. Fournès, G. Graveriau, and J. Etourneau, Investigation by ¹¹⁹Sn Mössbauer spectroscopy and electrical resistivity measurements of U₂M₂Sn stannides (M = Fe, Co, Ni, Ru, Rh, Pd), *J. Alloys Compd.* **203**, 29 (1994).
- [9] L. Havela, V. Sechovský, P. Svoboda, H. Nakotte, K. Prokeš, F. R. de Boer, A. Seret, J. M. Winand, J. Rebizant, J. C. Spirlet, A. Purwanto, and R. A. Robinson, Magnetism in U₂T₂X compounds, *J. Magn. Magn. Mater.* **140-144**, 1367 (1995).
- [10] H. Nakotte, A. Purwanto, R. A. Robinson, L. Havela, V. Sechovsky, L. J. C. Pereira, A. Seret, J. Rebizant, J. C. Spirlet, and F. Trouw, Hybridization effects in U₂T₂X compounds: Magnetic structures of U₂Rh₂Sn and U₂Ni₂In, *Phys. Rev. B* **53**, 3263 (1996).
- [11] S. Mašková, L. Havela, A. Kolomiets, A. V. Andreev, H. Nakotte, J. Peterson, K. Miliyanchuk, Y. Skourski, S. Yasin, S. Zherlitsyn, and J. Wosnitza, Onset of magnetic order in U(Ni_{1-x}Fe_x)₂Sn-H, *J. Korean Phys. Soc.* **62**, 1542 (2013).
- [12] K. Kindo, T. Fukushima, T. Kumada, F. R. de Boer, H. Nakotte, K. Prokeš, L. Havela, V. Sechovský, A. Seret, J. M. Winand, J. C. Spirlet, and J. Rebizant, Electronic properties of U₂Ni₂Sn, *J. Magn. Magn. Mater.* **140-144**, 1369 (1995).
- [13] R. P. Pinto, M. M. Amado, M. A. Salgueiro, M. E. Braga, J. B. Sousa, B. Chevalier, F. Mirambet, and J. Etourneau, Transport and magnetic properties of U₂Ni₂Sn and U₂Co₂Sn, *J. Magn. Magn. Mater.* **140-144**, 1371 (1995).
- [14] L. Havela, V. Sechovský, F. R. de Boer, E. Brück, and H. Nakotte, Magnetic anisotropy in UTX compounds, *Physica B* **177**, 159 (1992).
- [15] F. Bourée, B. Chevalier, L. Fournès, F. Mirambet, T. Roisnel, V. H. Tran, and Z. Zolnierok, Crystal and magnetic structures of U₂Ni₂Sn investigated by neutron diffraction and ¹¹⁹Sn Mössbauer spectroscopy, *J. Magn. Magn. Mater.* **138**, 307 (1994).
- [16] S. Mašková, A. V. Andreev, Y. Skourski, S. Yasin, D. I. Gorbunov, S. Zherlitsyn, H. Nakotte, K. Kothapalli, F. Nasreen, C. Cupp, H. B. Cao, A. Kolomiets, and L. Havela, U₂Ni₂Sn and the origin of magnetic anisotropy in uranium compounds, *Phys. Rev. B* **99**, 064415 (2019).
- [17] L. M. Sandratskii, S. Maskova, L. Havela, M. Divis, and K. Carva, Complex interplay of magnetic interactions in 5f-electron systems: The case of U₂Ni₂Sn, *Phys. Rev. B* **101**, 184433 (2020).
- [18] P. J. W. Moll, Focused ion beam microstructuring of quantum matter, *Annu. Rev. Condens. Matter Phys.* **9**, 147 (2018).
- [19] N. Fujiwara, T. Matsumoto, K. Koyama-Nakzawa, A. Hisada, and Y. Uwatoko, Fabrication and efficiency evaluation of a hybrid NiCrAl pressure cell up to 4 GPa, *Rev. Sci. Instrum.* **78**, 073905 (2007).
- [20] K. Murata *et al.*, Pt resistor thermometry and pressure calibration in a clamped pressure cell with the medium, Daphne 7373, *Rev. Sci. Instrum.* **68**, 2490 (1997).
- [21] D. Staško, J. Prchal, M. Klicpera, S. Aoki, and K. Murata, Pressure media for high pressure experiments, Daphne Oil 7000 series, *High Press. Res.* **40**, 525 (2020).
- [22] A. Hammersley, Program Fit2D (Version: V12.077), ESRF (2009).
- [23] L. Lutterotti, Total pattern fitting for the combined size-strain-stress-texture determination in thin film diffraction, *Nucl. Instrum. Methods Phys. Res. B* **268**, 334 (2010).
- [24] K. Koepf and H. Eschrig, Full-potential nonorthogonal local-orbital minimum-basis band-structure scheme, *Phys. Rev. B* **59**, 1743 (1999); www.fplo.de.
- [25] K. Schwarz, P. Blaha, and G. K. H. Madsen, Electronic structure calculations of solids using the WIEN2K package for materials sciences, *Comput. Phys. Commun.* **147**, 71 (2002); www.wien2k.at.
- [26] K. Schwarz, DFT calculations of solids with LAPW and WIEN2k, *J. Solid State Chem.* **176**, 319 (2003).
- [27] J. Kuneš, P. Novák, M. Diviš, and P. M. Oppeneer, Magnetic, magneto-optical, and structural properties of URhAl from first-principles calculations, *Phys. Rev. B* **63**, 205111 (2001).
- [28] J. P. Perdew and Y. Wang, Accurate and simple analytic representation of the electron-gas correlation-energy, *Phys. Rev. B* **45**, 13244 (1992).
- [29] J. P. Perdew, K. Burke, and M. Ernzerhof, Generalized Gradient Approximation Made Simple, *Phys. Rev. Lett.* **77**, 3865 (1996).
- [30] J. P. Perdew, A. Ruzsinszky, G. I. Csonka, O. A. Vydrov, G. E. Scuseria, L. A. Constantin, X. Zhou, and K. Burke, Restoring the Density-Gradient Expansion for Exchange in Solids and Surfaces, *Phys. Rev. Lett.* **100**, 136406 (2008).
- [31] Z. Wu and R. E. Cohen, More accurate generalized gradient approximation for solids, *Phys. Rev. B* **73**, 235116 (2006).
- [32] L. Havela, V. Sechovský, K. Prokeš, H. Nakotte, E. Brück, and F. R. de Boer, Magnetoresistance in actinide and lanthanide intermetallics, *J. Alloys Compd.* **207-208**, 249 (1994).
- [33] N. F. Mott, Conduction in non-crystalline systems IX. the minimum metallic conductivity, *Philos. Mag.* **26**, 1015 (1972).
- [34] J. H. Mooij, Electrical conduction in concentrated disordered transition-metal alloys, *Phys. Status Solidi A* **17**, 521 (1973).
- [35] B. S. Chandrasekhar and J. K. Hulm, The electrical resistivity and super-conductivity of some uranium alloys and compounds, *J. Phys. Chem. Solids* **7**, 259 (1958).

- [36] L. Havela, J. Hrebik, and J. Sternberk, The study of electrical and magnetic properties of the system $\text{UFe}_2\text{-UNi}_2$, *Acta Phys. Slovaca* **31**, 145 (1981).
- [37] G. Hilscher and V. Sechovsky, The origin of magnetism in UNi_2 - a simple band approach, *Solid State Commun.* **40**, 881 (1981).
- [38] L. Havela, V. Sechovsky, K. Prokes, H. Nakotte, H. Fujii, and A. Lacerda, Giant magnetoresistance effects in $5f$ -materials, *Physica B* **223-224**, 245 (1996).
- [39] K. Prokeš, H. Nakotte, E. Brück, F. R. de Boer, L. Havela, V. Sechovský, P. Svoboda, and H. Maletta, Anisotropic magnetic and transport properties of UNiGe , *IEEE Trans. Magn.* **30**, 1214 (1994).
- [40] L. Havela, M. Paukov, V. Buturlim, I. Tkach, D. Drozdenko, M. Cieslar, S. Maskova, M. Dopita, and Z. Matej, Electrical resistivity of $5f$ -electron systems affected by static and dynamic disorder, *Phys. Rev. B* **95**, 235112 (2017).
- [41] D. Laffargue, F. Bourée, B. Chevalier, T. Roisnel, P. Gravereau, and J. Etourneau, Crystal and magnetic structures of the ternary stannides $\text{U}_2\text{Pd}_{2+y}\text{Sn}_{1-y}$, *J. Magn. Magn. Mater.* **170**, 155 (1997).
- [42] H. Yamada and S. Takada, Magnetoresistance of antiferromagnetic metals due to s - d interaction, *J. Phys. Soc. Jpn.* **34**, 51 (1973).
- [43] K. Kadowaki and S. B. Woods, Universal relationship of the resistivity and specific heat in heavy-Fermion compounds, *Solid State Commun.* **58**, 507 (1986).
- [44] A. Ponchet, J. M. Mignit, A. de Visser, J. J. M. Franse, and A. Menovsky, Depression of spin fluctuations in UPt_3 at very high pressures, *J. Magn. Magn. Mater.* **54-57**, 399 (1986).
- [45] L. Havela, A. V. Kolomiets, A. V. Andreev, J.-C. Griveau, F. Honda, and Z. Arnold: Extended stability range of the non-Fermi liquid phase in UCoAl , *J. Phys.: Condens. Matter* **30**, 385601 (2018).
- [46] I. N. Goncharenko, J.-M. Mignot, V. A. Somenkov, J. Rossat-Mignod, and O. Vogt, Magnetic phase diagram of UAs at very high pressures up to 50 kbar, *Physica B* **199-200**, 625 (1994).
- [47] D. Laffargue, Ph. D. thesis, University of Bordeaux I (1997).
- [48] S. Mašková, L. Havela, S. Daniš, A. Llobet, H. Nakotte, K. Kothapalli, R. Černý, and A. Kolomiets, Impact of hydrogen absorption on crystal structure and magnetic properties of geometrically frustrated $\text{Nd}_2\text{Ni}_2\text{In}$, *J. Alloys Compd.* **566**, 22 (2013).
- [49] S. Mašková, A. M. Adamska, L. Havela, N.-T. H. Kim-Ngan, J. Przewoźnik, S. Daniš, K. Kothapalli, A. V. Kolomiets, S. Heathman, H. Nakotte, and H. Bordallo, Lattice anisotropy in uranium ternary compounds: UTX, *J. Alloys Compd.* **522**, 130 (2012).
- [50] P. Estrela, Ph. D. thesis, University of Amsterdam, 2000.
- [51] J. Prchal, V. Buturlim, J. Valenta, M. Dopita, M. Divis, I. Turek, L. Kyvala, D. Legut, and L. Havela, Pressure variations of the $5f$ magnetism in UH_3 , *J. Magn. Magn. Mater.* **497**, 165993 (2020).
- [52] H. H. Hill, The early “actinides”: The periodic system’s f electron transition metal series, in *Plutonium 1970 and Other Actinides*, edited by W. N. Miner (AIME, 1970), pp. 1–19.
- [53] www.mgml.eu.